Bulletin of the Seismological Society of America, Vol. 105, No. 6, pp. 2871–2884, December 2015, doi: 10.1785/0120150131

The Cardston Earthquake Swarm and Hydraulic Fracturing of the Exshaw Formation (Alberta Bakken Play)

by Ryan Schultz, Shilong Mei, Dinu Pană, Virginia Stern, Yu Jeffrey Gu, Ahyi Kim, and David Eaton

Abstract More than 60 small earthquakes (M_L 0.7–3.0) were detected from December 2011 to March 2012 north of Cardston, Alberta, an area with little evidence for previous seismic activity. The timing of these events closely correlates (> 99.7% confidence) with hydraulic fracturing completions of the Devonian–Mississippian-age Exshaw Formation at a nearby horizontal well. Unanimous waveform multiplicity within the swarm suggests that the events share a similar origin and source mechanism. This observation is corroborated by the point-like collocation of hypocenters within the crystalline basement during robust, double-difference relocations. Furthermore, the presence of a pre-existing fault is confirmed via formation-top offset mapping and interpreted to be a Late Cretaceous extensional fault. The confirmation of this fault at depth provides a plausible pathway for rapid hydraulic communication from the fracturing interval into the crystalline basement. Consistent with structural interpretations and available stress information, moment tensor inversion of the largest magnitude event (M_w 3.0) indicates reactivation of a basement fault with normal slip. We conclude that the genesis of this earthquake swarm was likely caused by increased pore pressure, within the basement fault, as a result of fracturing stimulation.

Online Material: Figure showing frequency–magnitude distribution of earthquakes, and table of the velocity models used in the study.

Introduction

Because of their low permeabilities, kerogen-rich shale has historically been regarded as uneconomical hydrocarbon reservoirs, despite their vast reserves. In the past, conventional operations targeted more easily produced, permeable reservoirs with hydrocarbon resources trapped in geologic structures. More recently though, hydraulic fracturing (HF) techniques have been utilized to stimulate production from low-permeability formations, such as the Barnett, Marcellus, and Fayetteville shales, to directly access their hydrocarbon potential. During HF treatments, pore pressure is increased and surpasses the least principal stress, thus propagating tensile failures throughout the rock matrix. This fracture network provides pathways for fluid migration, allowing for the exploitation of previously uneconomical reservoirs (King, 2010) or the restimulation of wells with declining productivity. In recent years, HF technologies have become more sophisticated, with developments in (1) slickwater fracturing, the inclusion of chemical additives like friction reducers, acids, biocides, and surfactants to HF fluid to better fracture the target formation and deliver proppant to maintain permeability; (2) horizontal drilling coupled with staged treatment schemas designed to increase fracture network complexity and shale-to-fracture contact area; and (3) diagnostics, such as tiltmeter fracture mapping, microseismic monitoring, borehole image logging, or radioactive tracers, to better model and thus optimize completions for maximum productivity. Development of shale gas resources has unlocked more than 7000 trillion cubic feet of newly recoverable gas worldwide (U.S. Energy Information Administration, 2013).

In contrast to the economic benefits of HF, there has also been increased concern regarding unique environmental challenges. For example, flowback water (Gregory *et al.*, 2011) from completions contains slickwater chemical additives, clays, and various total dissolved solids. Often, management strategies for flowback water have focused on disposal via deep injection wells. However, it has been well documented that disposal wells have the potential to induce earthquakes (e.g., Healy *et al.*, 1968) under tectonically favorable conditions. Although only a small fraction of disposal wells are observed to induce earthquakes, cumulatively the disposal of waste fluid into deep injection wells has been proposed as an explanation for the recently increased seismic hazard in the central United States (Ellsworth, 2013). Even

rarer, in a few cases seismicity has been directly linked to HF operations, such as in Lancashire, United Kingdom (Clarke *et al.*, 2014); the Eola field, Oklahoma (Holland, 2013); the Horn River and Montney basins, British Columbia (BC Oil and Gas Commission, 2012, 2014); Harrison County, Ohio (Friberg *et al.*, 2014); Poland township, Ohio (Skoumal *et al.*, 2015); and Crooked Lake, Alberta (Schultz, Stern, Novakovic, *et al.*, 2015; Eaton and Babaie Mahani, 2015).

Recently, increased capacity to monitor seismicity in the western Canada sedimentary basin (WCSB) has allowed for the better understanding of earthquakes in the region (Stern *et al.*, 2013). In fact, this article concerns a swarm of earthquakes in southwestern Alberta, Canada, which we argue is directly linked to nearby HF operations. Our argument, and the flow of this article, follows the criteria of Davis and Frohlich (1993). First, we will familiarize the reader with the setting and operations of the well we purport to have induced the swarm. Next, we highlight the unexpected nature of the swarm, followed by establishing a clear temporal correlation between HF activities and respondent seismicity. Furthermore, we utilize bootstrapped double-difference event relocations to robustly determine hypocenter geometry and compare these results to horizontal well trajectory. Seismic constraints on the fault orientation and mechanism are inferred by a regional moment tensor inversion and are subsequently compared to regional and local stress data. These arguments are accomplished by using continuous waveform data amalgamated from various regional networks (Schultz, Stern, Gu, and Eaton, 2015), including the Canadian National Seismic Network, the Montana Regional Seismic Network (D'Alessandro and Stickney, 2012), the Canadian Rockies and Alberta Network (Gu *et al.*, 2011), and the Alberta Telemetered Seismic Network (Eaton, 2014). We supplement seismic features of the swarm by characterizing the local, faulted geology through interpretation of logged formation topography and inferred discontinuities. Last, we review the geomechanics of earthquake induction and compare our results to similar and contrasting case studies. We conclude that the anthropogenic induction of these earthquakes due to HF operations is their most likely cause.

The Cardston Horizontal Well

In southern Alberta and Montana, the Big Valley and Stettler carbonates, medial Exshaw dolomitic siltstones, and basal Banff and Exshaw shales collectively comprise an unconventional, tight oil resource (Zaitlin *et al.*, 2010, 2011). This play has been coined the "Alberta Bakken," by industry in reference to the stratigraphically equivalent Bakken Formation in the nearby Williston Basin to the southwest (MacQueen and Sandberg, 1970). Traditionally, the Devonian–Mississippian aged Exshaw Formation has been regarded as a source rock for more conventional oil reservoirs, with the best prospects in the upper portion of the underlying Stettler Formation. Poorer prospects of the medial Exshaw, as a conventional reservoir, have been attributed to low permeability and thin interval. However, recent developments of HF technologies have made it economically feasible to exploit this shale oil resource with preliminary, median estimates of the in-place oil at 24.8 billion barrels (Rokosh *et al.*, 2012).

This article focuses on one well in the Ninastoko Field, developed to exploit the Exshaw shale oil, ~13 km north of the town of Cardston in southern Alberta (Fig. 1). For brevity, we will refer to this well as the Cardston horizontal well (CHW). The CHW is a multistaged horizontal well completed in December 2011. CHW trajectory begins vertically until the "build" section just above the target Exshaw Formation, where the wellbore transitions to horizontal with a heel-to-toe distance of ~1.6 km at an azimuth of 320°; in total, the entire well bore length is 4306 m. Locally, the Exshaw Formation is logged at ~2845 m depth and 11 m thickness. Treatment of the CHW was completed in 10 individual stages and 34 acid-spotted perforation intervals. After perforation, hybrid water HF treatments were applied to enhance the permeability of the target reservoir rock. Average mean pressures, pumping rates, total pumped fluid volume, and proppant weight in well for HF treatment stages are 73.9 MPa, 5.5 m^3/min, 716 m^3, and 150 tonnes, respectively.

The Cardston Swarm: Waveforms and Time Series Correlations

Coincident with the timing and proximity of HF operations at the CHW, a swarm of earthquakes was recorded on regional arrays (Fig. 1), the largest of which approached M_L 3.0. This swarm of events, referred to as the Cardston Swarm (CS), is unusual for the seismic history of the region (e.g., Stern *et al.*, 2013). For example, the Natural Resources Canada earthquake catalog (Earthquakes Canada, 2014) contains three events within a 25 km radius of the CHW, from 1985 until HF initiation. We note that the whole waveform characteristics (Reyes and West, 2011) of CS versus pre-HF events differ significantly, suggesting differences in source location or mechanism. On the other hand, a high degree of similarity is observed in all CS events; in comparison to the CS beam paired with individual traces, the average correlation coefficient is greater than 0.92 within a frequency bandwidth of 0.5–8.0 Hz. This information places stringent constraints on individual event perturbations to the source mechanism and spatial separation of CS events, as compared to the swarm average.

We take advantage of waveform multiplicity by employing a multichannel, cross-correlation search algorithm (Schaff, 2008) to extend the minimum magnitude detection threshold beyond conventional methods. Our search time frame buffers the conventionally detected events by roughly two years, starting in 2010 through 2013. From this extended catalog, we observe more than 60 CS events that are primarily recorded on the first week of December 2011 with smaller, secondary events occurring after completion of the CHW in February and March of 2012 (Fig. 2a). Interestingly, no events are detected before, or long after, HF activ-

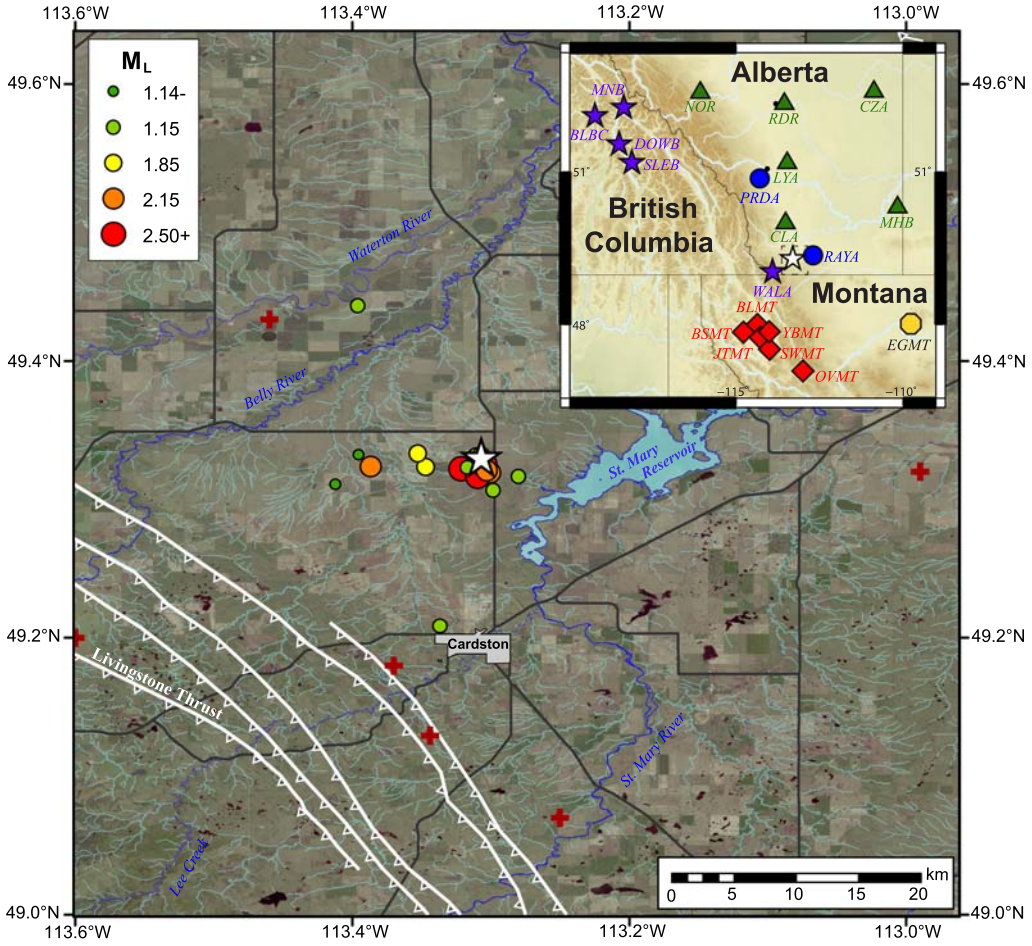

Figure 1. Geographic locations of earthquakes relevant to this study. Crosses in the larger map represent the spatial distribution of previous seismicity, circles denote the conventionally relocated earthquakes in the Cardston Swarm (CS), and the star represents a nearby horizontal well. The inset map indicates the location of the study area regionally (dashed box) and the locations of the Canadian National Seismic Network (stars), the Montana Regional Seismic Network (diamonds), the Canadian Rockies and Alberta Network (triangles), the Alberta Telemetered Seismic Network (circles), and USArray (hexagon) stations. Locations of known previously mapped faults have been superimposed for reference (Hamilton *et al.*, 2012), and portions of this figure utilized the program Generic Mapping Tools (Wessel and Smith, 1998). The color version of this figure is available only in the electronic edition.

ities, indicating that events are restricted to this period and that our rate for false positive detections is negligible.

When compared to operations at the CHW, we observe repeated trends in primary seismicity synchronized with stages 5, 6, and 7 (Fig. 2b): midway through each stage, events are initiated and occur frequently for a period comparable to the most recent stimulation duration, with events occurring less frequently during post-HF periods. Seismicity preceding later stages (8+) no longer adheres to this pattern, occurring more sporadically and only during post-HF moments. Additionally, seismic events are detected during a period two to three months after completion at the CHW. We begin to quantify the relationship between seismic activity and HF operations at later stages (5+) by comparing cumulative seismic moment release and total injection volume (McGarr, 2014). In this study, seismic moments are estimated from a scaling relationship. A linear regression of these data (Fig. 3a) has a high goodness of fit (R^2 of 0.895), suggesting a causal relationship between these two processes.

Lastly, we use signal-processing techniques to determine the statistical confidence in the relationship between seismicity in the CS and operations at the CHW. First, the extended seismic catalog is truncated based on an estimate of its magnitude of completeness. We compute the magnitude of completeness as the cut-off magnitude that maximizes the goodness of fit to the Gutenberg–Richter frequency–magnitude data using the maximum-likelihood method (Aki, 1965; Shi and Bolt, 1982). These techniques provide a best estimate of seismic *b*-value as 1.11 ± 0.17 when coupled with a magnitude of completeness of 1.8 M_L (Ⓔ Fig. S1, available in the electronic supplement to this article). Second, the truncated catalog is cross correlated with the average HF pressure for each stage, because detailed pressure treatment curves were unavailable. We find that seismicity is best correlated to CHW treatments at lag times between 1.5 and 3.0 hrs (Fig. 3b), similar to the HF duration of stages 5 and 6 (3 hrs). Flanking correlation peaks are likely due to the approximately daily periodicity of

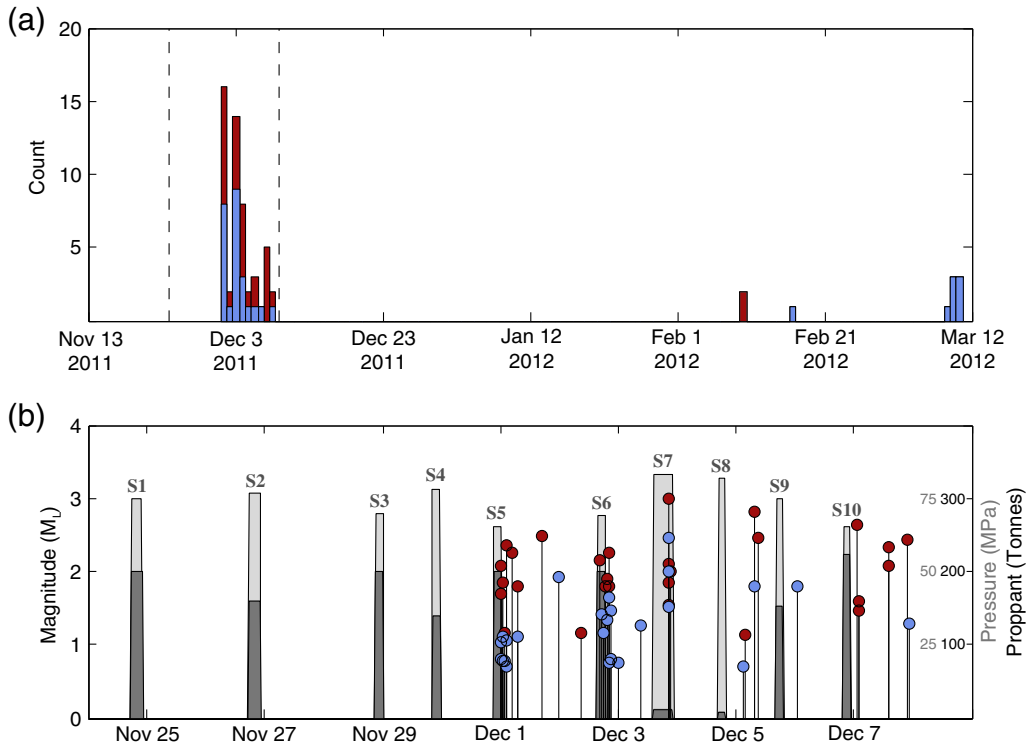

Figure 2. (a) Histogram of the located seismicity in the CS (upper, darker bars) and the extended catalog from cross-correlation methods (lower, lighter bars); hydraulic fracturing (HF) activity is bounded within the dashed lines. (b) Temporal distribution of earthquake magnitudes for both located seismicity (upper, darker circles) and cross-correlation detected seismicity (lower, lighter circles) compared to average treatment pressure (gray filled area) and proppant delivered in the formation (dark gray) for individual HF stages (labeled numerically). The color version of this figure is available only in the electronic edition.

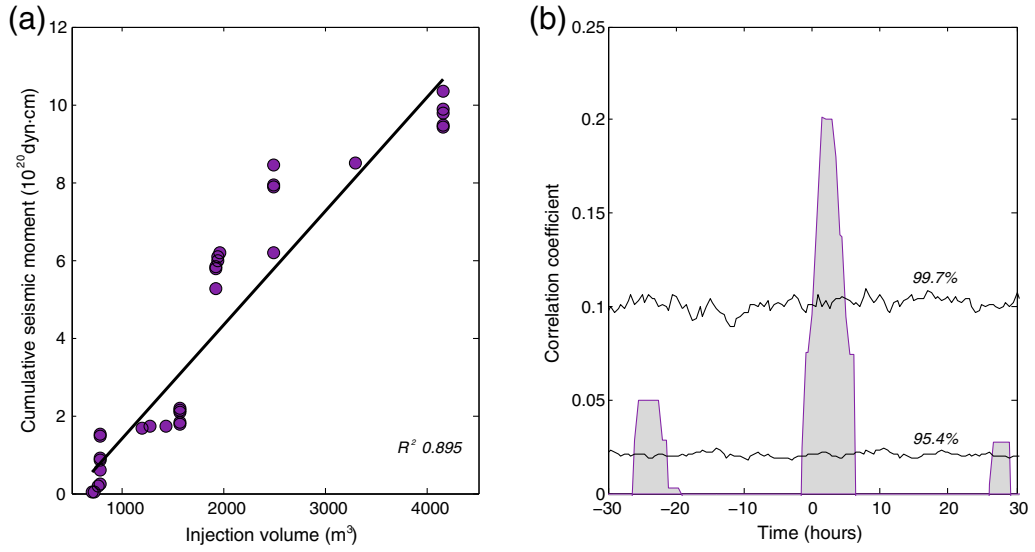

Figure 3. Correlations between HF operations at Cardston horizontal well (CHW) and seismic activity at the CS. (a) Scatterplot of cumulative seismic moment versus total injected fluid volume (circles) for later (5+) stages and the best fit to the data (black line). (b) Cross correlation of catalog ($M_L > 1.8$) and average HF pressure time series (gray curve). Confidence intervals (black lines) are determined by reshuffling tests and are labeled with their statistical significance. The color version of this figure is available only in the electronic edition.

HF operations at the CHW. Last, the statistical confidence in the time-series analysis is quantified by performing random reshuffling tests, analogous to the methodology prescribed by Telesca (2010). This analysis indicates that the dominant correlation between CS seismicity and CHW average HF pressure curves has a confidence greater than 99.7% (Fig. 3b).

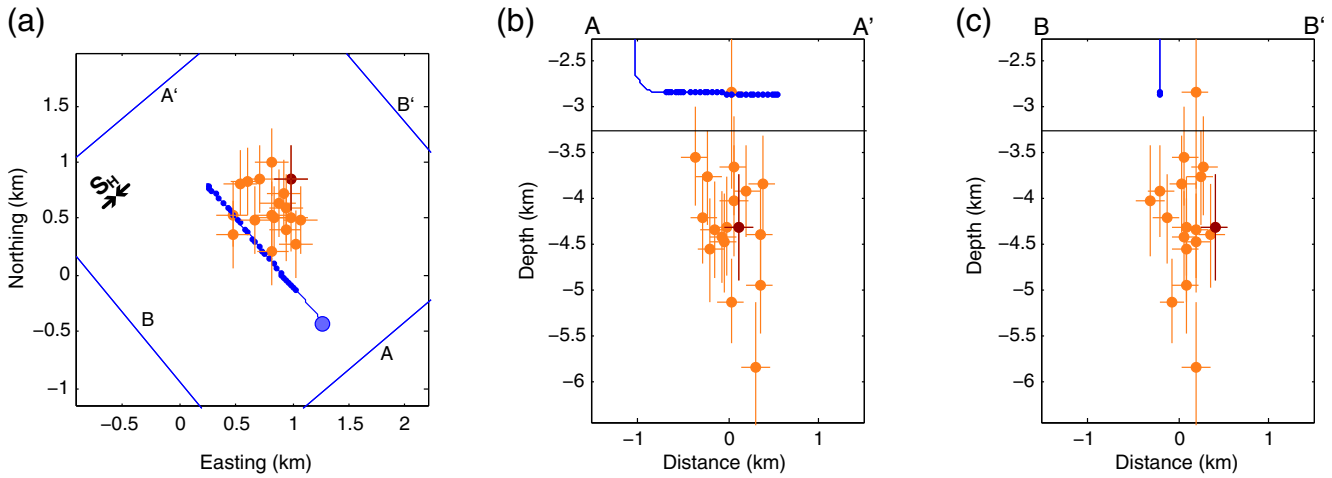

Figure 4. Robust double-difference relocations of CS events using bootstrap and model perturbations. Cross hair span indicates error ellipses (1 standard error) as determined from the bootstrapped distribution. Degree of event consistency in model perturbations is depicted: the lighter cross hairs agree within 2 standard errors, and the darker cross hair agrees within 1. (a) Map view of CS epicenters (circles with cross hairs) in relation to the CHW surface location (larger circle) and perforation intervals (smaller circles). (b) Depth cross section trending approximately southeast to northwest, from A to A'. (c) Depth cross section trending perpendicular to CHW azimuth (and parallel with regional maximum horizontal stress S_H; Reiter *et al.*, 2014). The majority of well-relocated events are within the Precambrian (denoted by horizontal line). The color version of this figure is available only in the electronic edition.

Robust Event Relocations

The observation of repeated waveforms in the CS suggests that these events are, to a degree, collocated and share a source mechanism. For example, Baisch *et al.* (2008) found that correlation coefficients of 0.90 result in spatial separations no larger than a half wavelength. In this study, we employ a double-difference location algorithm (Waldhauser and Ellsworth, 2000) to invert hypocenter locations and examine the spatial distribution of the CS. Initial hypocenters are determined from a relocation of CS events with a local velocity model (Fig. 1); our local velocity model is determined from both nearby well log data, local receiver function studies (Chen *et al.*, 2015), and CRUST1.0 (Laske *et al.*, 2013) (Ⓔ Table S1). During conventional inversions, the depth parameter is assumed to be 3 km, which we consider a reasonable starting guess given the temporal correlation to CHW activities and the logged depth of the Exshaw Formation (~2845 m). Within the CS there are more than 25 located events, and their phase arrival pairings result in more than 2300 and 2100 P and S catalog differential times, respectively. Cross-correlation differential lag times were computed by windowing 0.5 s before and 1.0 s after the hand-picked phase arrivals, producing more than 1700 P and 1100 S waveform differential lags.

Although hypoDD performs well in discerning the relative geometry of earthquakes, it is generally understood that it may retain systematic bias in the cluster's absolute location (Waldhauser and Ellsworth, 2000). To determine the robustness of CS hypocenters, we first begin by performing a bootstrap test to our dataset (Efron and Tibshirani, 1986). First, we take a subset of our catalog to destabilize the output, 10% of the initial earthquake locations are randomly removed before the double-difference inversion. This process is iterated 1000 times so that we may examine the variation in each individual event location as a statistical distribution. We define the robust hypocenter as the modal value measured directly from the distribution; an event location is said to be robust if the location parameter distributions are well behaved (e.g., are not multimodal).

By performing a bootstrap test, we more faithfully reproduce the true geometry and errors of hypocentral parameters and ensure the stability of our solutions (Efron and Tibshirani, 1986). However, relative unknowns in the velocity model can also adversely influence event locations. To test the degree of influence from the velocity model, we perturb our model. The bootstrap process is repeated for two additional velocity models, which have been systematically biased 10% faster or slower. Subsequently, we compare these results to the unperturbed catalog. Events are said to be consistent if the robust results from all three velocity models agree within either one or two standard errors.

After ensuring the fidelity, consistency, and robustness of 18 hypocenter solutions, we observe a strong spatial clustering of CS events (Fig. 4). In terms of relative geometry, events are almost exclusively collocated with no clear indication of lineations or trends and are typically (1 standard error) within 200, 250, and 650 m of the centroid for longitude, latitude, and depth, respectively. Similarly, the mean values of hypocenter standard errors are 150, 300, and 600 m for longitude, latitude, and depth, respectively. This provides a potential explanation for the lack of observed structure in the CS hypocenter geometry; likely, the true structure of CS events is on a scale smaller than the network's resolving

power and our observed "structure" is simply the statistics of error. Unfortunately, this result also precludes our ability to examine the time dependence of CS structure. Regarding absolute positioning, the CS centroid is within close lateral proximity of the CHW (Fig. 4a). At the closest approach to the CHW (~450 m from the well toe, near stage 4), there is a spatial separation of ~300 m perpendicular from the well trajectory. However, we observe that the average depth (4.3 km) of the CS events is biased below the CHW trajectory (2850 m). We note that individual events span depths no shallower than the CHW and are largely centered within the crystalline basement (Fig. 4b,c).

Moment Tensor Inversion

Earthquake focal mechanisms describe the radiation pattern of seismic waves propagating from slip on a fault. To investigate the source mechanism of the CS, we utilize a time-domain, waveform inversion routine (Dreger, 2003) coupled with a frequency–wavenumber integration routine (Saikia, 1994) to solve for the regional moment tensor. Our data is beam averaged over the CS to increase signal-to-noise ratio, scaled to the amplitude of the largest event, and band-pass filtered from 0.35 to 0.80 Hz for stations RAYA, WALA, CLA, and LYA (see Fig. 1). Filter corners were chosen in an interval that maintains a good signal-to-noise ratio from the interfering microseisms, and before the empirically observed earthquake corner frequency. Both synthetic and recorded ground displacements are tapered to constrain fitting to first-arriving body waves and mitigate complexities from crustal multiples.

It is recognized that the quality of waveform matching during moment tensor inversion can trade off with input parameters, such as hypocenter location. Hence, we perform moment tensor inversions for various depths (Fig. 5a) to determine the optimal source depth, the most poorly constrained hypocenter parameter. Best fits are observed when source depths are in the lower sedimentary units and upper crystalline basement. Given this overall consistency with double-difference results, hypocenter parameters from the double-difference results were used in all following moment tensor inversions. Next, we perform a bootstrap analysis (Efron and Tibshirani, 1986) by randomly perturbing station channel weight for 10^5 inversion realizations (Fig. 5b). Results from this bootstrap provide a measure of fit as a function in the source-type space (Vavryčuk, 2015). In this sense, our best-fit moment tensor is defined by the mean of more than 3000 moment tensors within the contour interval defined by a relative variance reduction greater than 90%; analogously, errors are defined by the standard deviation in the same contour interval.

Overall, we find that ground motions from the CS are best described by a moderate-size (3.0 ± 0.1 M_w), double-couple source, with minor contributions from isotropic (ISO) and compensated linear vector dipole (CLVD) components (0.70 ± 0.08, 0.16 ± 0.08, and -0.14 ± 0.09, respectively). We hesitate to make interpretations on the non-double-couple components, despite their potential for tensile mechanisms (e.g., Fischer and Guest, 2011; Rutledge *et al.*, 2013). Instead, it is likely these small non-double-couple components are simply the result of fitting ambient noise due to their opposing polarities and similar magnitudes. On the other hand, we find that the double-couple moment tensor is best interpreted as a normal fault with nodal planes defined by strikes $12° \pm 35°/203° \pm 34°$, dips $82° \pm 4°/9° \pm 8°$, and rakes $-92° \pm 40°/-78° \pm 38°$ (Fig. 5c,d).

Fault Detection and Geologic Constraints

Regional Tectonic Evolution

The studied area is in southern Alberta and part of the WCSB that forms a northeastward-tapering wedge of supracrustal rocks overlapping the Precambrian crystalline rocks of the North American craton (Price, 1994). The WCSB evolved in two main stages: (1) a Proterozoic to Middle Jurassic platform stage, correlated with the continental rifting that created the initial Cordilleran continental margin of the North American craton and, subsequently, the continental terrace wedge; and (2) a Late Jurassic to Early Eocene foreland basin stage, correlated with the accretion of allochthonous oceanic terranes (e.g., Beaumont *et al.*, 1993). These two successive tectonic settings are generally accepted, although, the timing of initiation of the rifted North American margin, foredeep, and fold-and-thrust belt are still controversial (Hildebrand, 2013).

During the second stage, in the late Middle Jurassic, the region became a foreland basin in front of the growing orogen to the west. Events leading to Cordilleran mountain building started in Middle Jurassic time as a result of collisions with eastward- and northeastward-drifting island arcs on the proto-Pacific lithosphere (e.g., Monger and Price, 2002). The upper-crustal tectonic elements (or allochthonous terranes) were juxtaposed over each other and over the western margin of the North American craton along a system of interleaved, northeast- and southwest-verging major thrust faults (Struik, 1988). Late Middle Jurassic to early Eocene deformation resulted in a thick stack of east-vergent, generally downward- and eastward-younging thrust slices in the Rocky Mountain fold-and-thrust belt (Pană and van der Pluijm, 2014). Flexural downwarping of the North American lithosphere as a result of tectonic loading in the Cordilleran orogen triggered subsidence in the Alberta basin, likely accommodated by brittle faults in the upper structural levels. Contraction was succeeded by transtension and extension during the middle Eocene.

As a result of its complex tectonic evolution, the structural framework of southern Alberta includes, from west to east, three major domains: the Rocky Mountain fold-and-thrust belt, the Alberta syncline, and the Sweetgrass arch. The eastern boundary of the Rocky Mountain fold-and-thrust belt is known as the eastern limit of Cordilleran deformation,

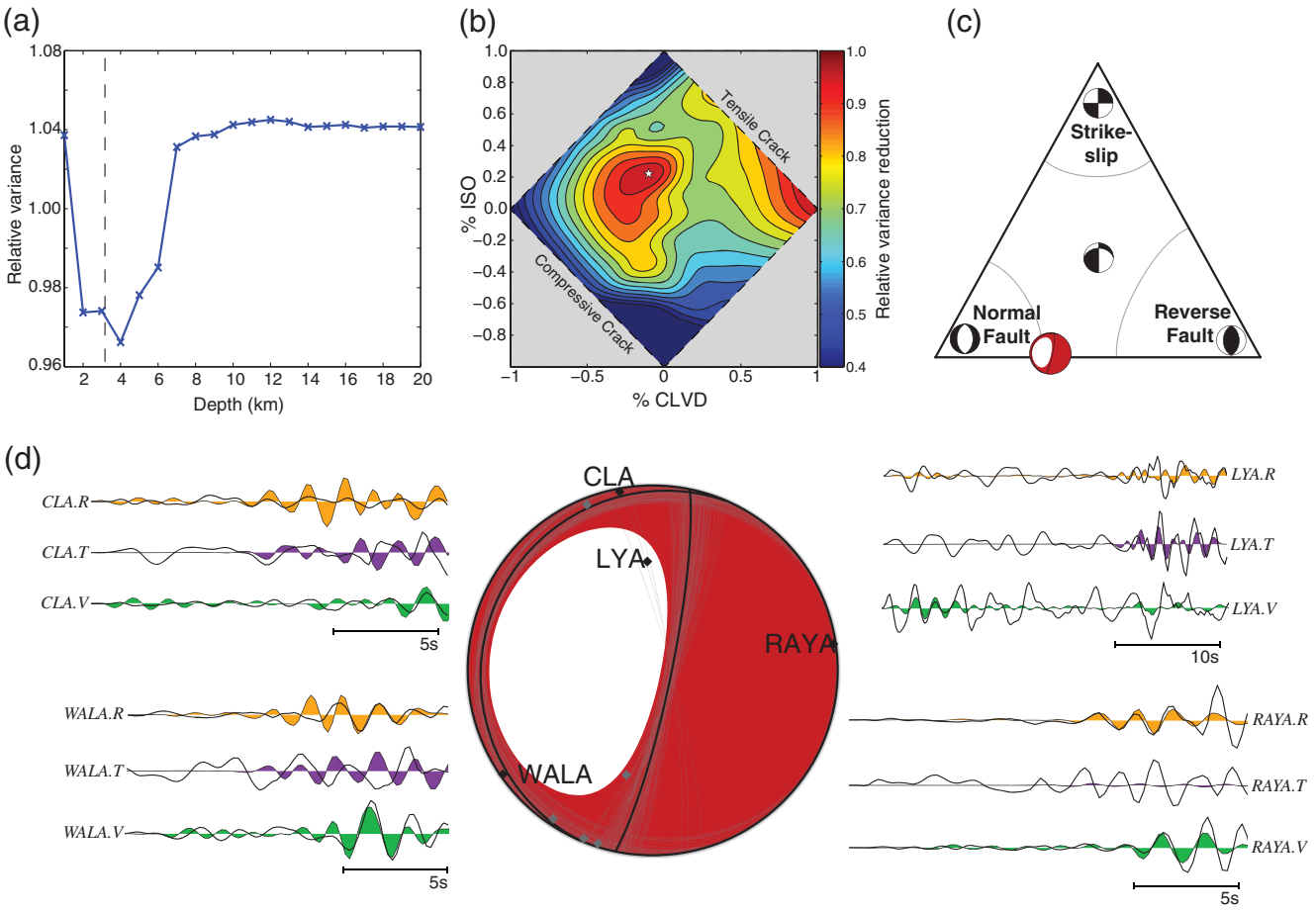

Figure 5. Results from time-domain moment tensor inversions. (a) Depth test results indicate the best fit of waveforms is obtained when the earthquake source is modeled within the basal sedimentary units or the shallow crystalline basement (boundary indicated by dashed line). (b) In the diamond CLVD–ISO plot (compensated linear vector dipole and isotropic, respectively) for all bootstrap realizations, respondent variance reductions are smoothed then contoured in this source-type space (0.05 intervals, see legend), and the peak value (white star) indicates the locale of best fit. (c) Ternary plot indicating faulting type from moment tensor decomposition (Frohlich, 2001): the best moment tensor solution (focal mechanism scaled to error bars) favors normal-faulting style, with a component of reverse. (d) Focal mechanism representation of the best moment tensor solution, with take-off angles labeled for individual stations (black diamonds). Nodal planes are indicated by strong black lines and surrounding lines (thin and gray) represent the 100 best-fit local bootstrap perturbations to the nodal planes. Surrounding ground displacement time series compare the fit of data (black lines) to synthetic (shaded area) for radial, transverse, and vertical components of the wavefield at each station (text labels). The color version of this figure is available only in the electronic edition.

arbitrarily traced on the east side of the structural triangle zone, which marks the eastern margin of the Foothills. However, in southern Alberta, imbrication and/or duplexing structures have been reported or inferred as far as 100 km to the east of the triangle zone. For example, Hiebert and Spratt (1996) suggested that the Monarch fault zone on Oldman River (Irish, 1968) may be a Laramide thrust fault localized along a pre-existing basement-controlled normal fault, based on seismic data. The strata underlying the Alberta Plains to the east dip gently to the south-southwest, except near the edge of the Foothills, where Paleocene strata are gently folded upward on the east flank of a structural triangle zone, forming the western limb of the Alberta syncline (e.g., Stockmal *et al.*, 2001). Extensional faults in this area add to the structural complexity; examples of such faults are the northwest-striking extensional faults noted along the banks of the Oldman River near Lethbridge (Russel and Landes, 1940) and extensional faults striking at 120°–128° in an area to the east of Fort Macleod (Wright *et al.*, 1994).

Faults Identified from Stratigraphic Data

In this section, we present the results of detailed mapping of the subsurface bedrock stratigraphy in the area of interest, in the vicinity of the CHW and CS. The main objective of the subsurface mapping was to identify and highlight offsets of formation tops that may have been caused by faulting. We selected and mapped three representative Late Cretaceous surfaces: the Lower Bearpaw flooding surface (LBFS), the top of the Milk River Formation (MRF), and the base of Fish Scales zone (BFSZ), as well as the top of Devonian–Mississipian-age Exhaw Formation. These regionally

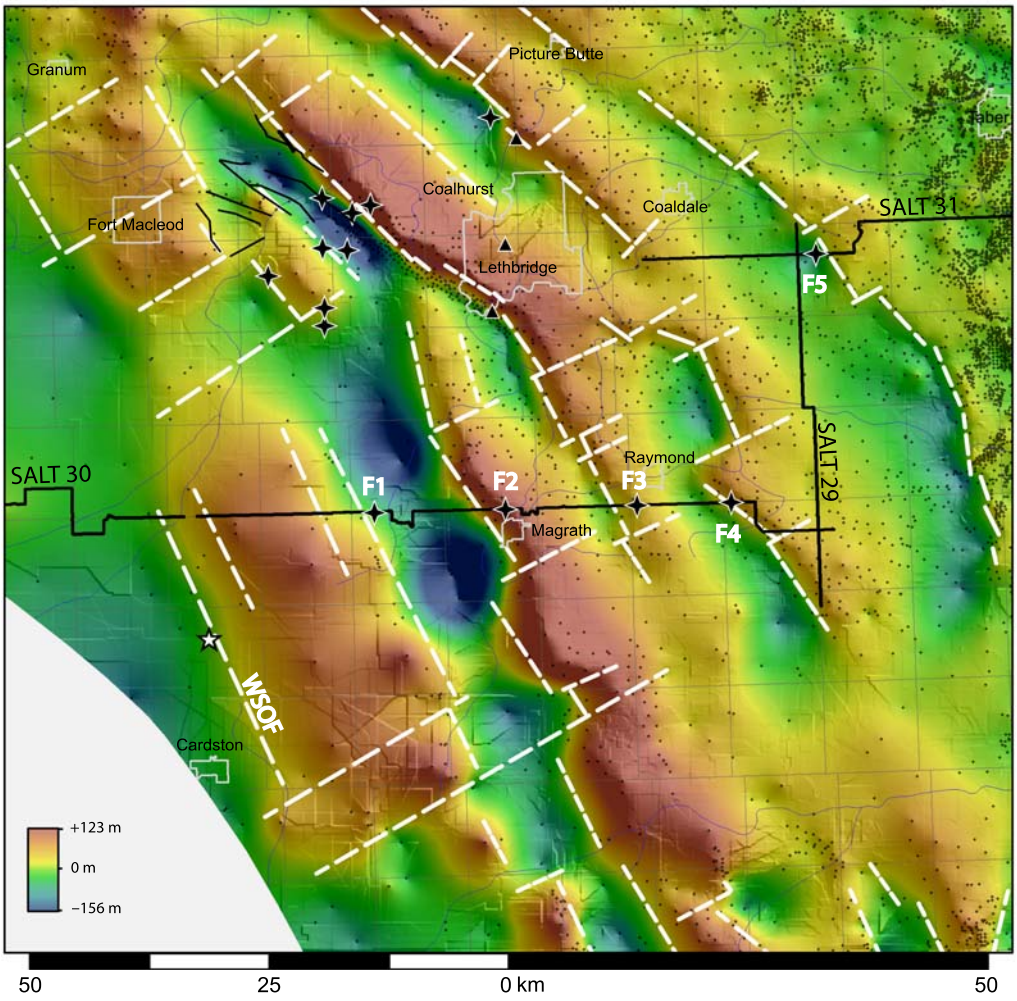

Figure 6. Formation-top offset map from the base of Fish Scales zone (BFSZ) (shaded background) in the region of the CHW (white, five-point star). Lineaments are inferred from steep gradients in the offset map and denoted by white dashed lines. The well locations used to constrain the offset surface are denoted by black dots, and municipalities are superimposed for geographic reference (light gray outlines). Seismic lines from the Lithoprobe Southern Alberta Lithospheric Transect are labeled by black lines, and the locations of faults interpreted from these seismic profiles by Lemieux (1999) are marked (black four-point stars and labeled F1–F5). Faults relevant to this study are identified in white text by their acronym in the text. Additional faults are included for the interest of the reader between Fort Macleod and Lethbridge and are denoted by unlabeled four-point stars (Lemieux, 1999), thin-black lines (Wright *et al.*, 1994; Hiebert and Spratt, 1996), and triangles (Russel and Landes, 1940). The color version of this figure is available only in the electronic edition.

extensive marine bedrock surfaces are assumed to have formed during sediment deposition on a roughly planar depositional surface; the effects of wave, tide, and currents ensured that these surfaces were smooth during deposition and thus can be consistently picked on well logs. More than 530, 2000, 4500, and 200 picks from publically available geophysical well logs have been used to define the LBFS, MRF, BFSZ, and Exshaw surfaces, respectively. Regional trends in formation tops, representing the combined effects of regional deposition, deformation, and compaction, are fit via a local polynomial interpolation, and then structural features/offsets are mapped from kriging of the regionally detrended data points. The results of the structural offset map are quality controlled by rejecting statistically large residuals or through verification of well log data. This process has been repeated for all selected bedrock surfaces (LBFS, MRF, BFSZ, and Exshaw) to both ensure consistency in the observed offsets at different stratigraphic levels and delineate trends with depth. Overall, the methodology used in this study allows the recognition of meter-scale formation-top offsets that are below the resolution limits of conventional seismic surveys (Mei, 2009a,b).

The application of this methodology in the investigated area, situated 52–140 km east of the Foothills triangle zone, resulted in the identification of numerous linear northwest–southeast-striking (130°–160°) offsets (Fig. 6). The strikes of these linear offsets are consistent with the local magnetic grain of the basement represented in the investigated area by the Archean Medicine Hat block (Ross and Eaton, 1999). In Figure 6, we have highlighted several offsets in stratigraphy,

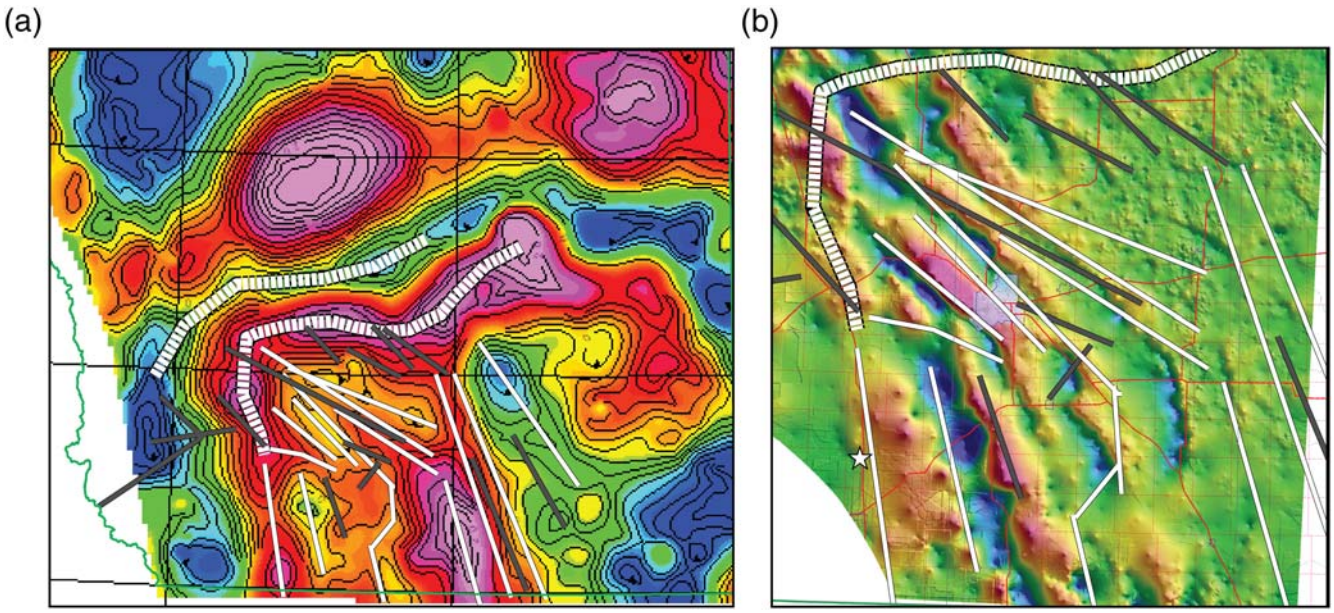

Figure 7. (a) Bouguer gravity anomaly map of southern Alberta with the third-order trend removed; faults inferred from both gravity data (solid white lines) and aeromagnetic data (solid gray lines) are superimposed. The dashed white lines place boundaries between basement domains. (b) The same basement faults inferred from potential field data are displayed in the context of the study region: the CHW (white star) is overlaid on a background indicating formation-top offset of the BFSZ (Fig. 6). The color version of this figure is available only in the electronic edition.

which correspond to five significant Late Cretaceous extensional faults extending into the Archean basement (F1–F5, Fig. 6), also depicted by the Lithoprobe Southern Alberta Lithospheric Transect (SALT) seismic-reflection data (Lemieux, 1999; Lemieux *et al.*, 2000). For example, one of our faults corresponds to the seismically identified F1 (Fig. 6), which was interpreted as a Laramide far-field inversion compressional fault overprinting an initial west-dipping extensional fault (Lemieux, 1999). In addition to confirming seismically identified faults (F1–F5), our offsets map highlights previously unrecognized structures.

Relevant to our study, a linear offset about 22 km to the west of F1 is recognized in all (LBFS, MRF, BFSZ, and Exshaw) offset maps and is herein referred to as the West Stand Off fault (WSOF) after the community of Stand Off. Similarly to F2, F3, and F5, steep basement fabrics appear to align directly with the position of the WSOF (fig. 5a of Lemieux, 1999). At a regional scale, the WSOF strikes at ~155°, roughly parallel to the linear offset F1. The location of identical offset trends generated for different stratigraphic units place rudimentary constraints on the dip angle of faults, and the WSOF is observed to dip steeply to the west at an angle no shallower than 50°. The vertical displacement on this fault decreases from 55 to 70 m at the depth of the Devonian–Mississippian Exshaw Formation, to 40–45 m at shallower depth of the Cretaceous BFSZ, MRF, and LBFS. This relatively small displacement, combined with its location at the data gap of SALT line 30 may represent the cause for the WSOF not being recognized in literature prior to our study.

Faults Inferred from Potential Field Data

Although F1–F5 are obvious throughout the sedimentary section and upper Archean basement, they are not clearly expressed throughout the entire crystalline basement (Lemieux, 1999). However, additional information on the underlying Archean Medicine Hat block of southern Alberta can be extracted from detailed processing of regional gravity and high-resolution aeromagnetic data compiled by the Geological Survey of Canada (e.g., Ugalde *et al.*, 2008). Bouguer anomaly maps represent the rock-density variations in the crust and asthenosphere, and lineaments in these maps are defined by gradient zones, alignment of separate local anomalies, aligned breaks, or discontinuities in the anomaly pattern (Fig. 7a). The lineaments extracted from these maps may represent vertical offsets across high-angle faults where rocks with different densities are juxtaposed (Lyatsky and Pană, 2003; Lyatsky *et al.*, 2004). Two such anomalous lineaments, traced along the center of two gravity highs and lows, are almost coincident with the location of the WSOF and F1 (Fig. 7b). The spatial relationships between faults inferred in the basement and those identified in the overlying sedimentary cover can be complicated by the different rheological properties of the different sequences (e.g., refraction through contrasting brittle carbonate and ductile shale successions). Consequently, although mechanically related, faults in the sedimentary cover (suprabasement faults) do not necessarily overlap their controlling intrabasement faults (e.g., Ross and Eaton, 1999).

A lineament trending ~167°, associated with the WSOF, can be traced just east of Cardston through the center of two

elongated high-density anomalies on the contoured Bouguer gravity data map and can be highlighted by data processing, such as the gravity map with third-order trend removed (Fig. 7b), the gravity map with automatic amplitude gain, and the map of the first vertical derivative of gravity data. The same lineament is easily identifiable along a high gradient linear zone on the horizontal gradient gravity map, total gradient of gravity data, and gravity data with vertical shadowgram superimposed. This lineament can also be identified on the map of magnetic data with superimposed vertical shadowgram (Lyatsky *et al.*, 2005). We suggest that this lineament derived from potential field data may represent faulting, and thus the WSOF would extend into the Archean basement, analogous to previously inferred extensional faults (F1–F5).

Overall, it appears that the WSOF was formed contemporaneously with F1–F5, during a widespread Late Cretaceous extension in southern Alberta. Furthermore, our interpretation is consistent with lithospheric downwarping marked by the westward transgression of the Bearpaw Sea, likely triggered by the massive Campanian tectonic loading in the fold-and-thrust belt (Pană and van der Pluijm, 2014).

Discussions

Traditionally the HF process is thought of as inducing a tensile mode of failure in the rock matrix. In reality, the process can be more complicated, involving both seismic and aseismic deformation. For example, it has been suggested that much of the seismic deformation is actually the result of shear dislocation along pre-existing, natural fractures (Maxwell and Cipolla, 2011; Yang *et al.*, 2013). Geomechanically, shear events are nucleated when the shearing stress surpasses the fault friction and cohesion. In this sense, shear dislocation can be induced by increasing pore pressure, hydraulically opening the fracture, and thus reducing the effective normal stress (e.g., Hubbert and Rubey, 1959). These events are often dubbed "microseismic" due to their small magnitudes (−4.0 to −0.5 M_w) and monitored to understand fracture growth during treatment stages (Warpinski *et al.*, 2012). However, inducing shear dislocation on larger, favorably oriented faults has also been observed during treatment (e.g., Maxwell *et al.*, 2010). Fault activation during HF poses risk for operators through economic waste. In cases with *a priori* knowledge of nearby faults, diversion strategies have been employed to minimize this risk (e.g., Waters *et al.*, 2009). In reality, potential faults are often blind or unknown; and, in some cases, real-time seismic monitoring systems have been able to successfully identity fault activation via anomalous spatial distribution or orientation of events, an abrupt increase in event magnitude, or change of observed *b*-value from 2 to 1 (Downie *et al.*, 2010; Wessels *et al.*, 2011). Despite these efforts, induced macroseismic events can still be large enough to be detected on regional networks or even felt, with numerous examples associated with HF (e.g., Friberg *et al.*, 2014; Schultz, Stern, Novakovic, *et al.*, 2015; Skoumal *et al.*, 2015), as well as geothermal and wastewater-disposal applications (e.g., Majer *et al.*, 2007; Kim, 2013; Schultz *et al.*, 2014).

In this section, we argue that the regionally observed CS seismicity are most likely HF-induced events and our results support a geologically plausible scenario that is consistent with induced seismicity. First, the observation of correlations between timing of CHW completions and CS seismicity provides credibility to the assertion of a causal link (Fig. 2). Figure 3a clearly shows a linear relationship between cumulative seismic moment release and total injection volume (McGarr, 2014). More rigorously, we demonstrated that HF operations and respondent seismicity were correlated to a confidence greater than 99.7% (Fig. 3b), with most events rupturing 1.5–3.0 hrs after HF stage initiation. Delays in seismicity are often observed on the order of years at disposal sites (e.g., Schultz *et al.*, 2014) and enhanced oil recovery waterflood operations (e.g., Horner *et al.*, 1994). This time delay can be explained as the propagation time of the fluid pressure front through porous strata to distant (10+ km), favorably oriented faults (Hsieh and Bredehoeft, 1981). Similar assertions have been made for HF-related seismicity (Davies *et al.*, 2013), albeit at shorter distances and delay times due to the smaller scale, increased permeability, and unsustained nature of fluid injection involved with HF. Analogously, we attribute the relatively brief delay to a nearby fault in communication with CHW treatment stages, a conjecture supported seismically by the laterally adjacent event relocations (Fig. 4a). Given the predilection of reservoir fluid flow along the maximum horizontal stress S_H (e.g., Chen *et al.*, 2011), alignment of CHW trajectory with S_H, and fracturing of the Exshaw to increase permeability, it is reasonable to expect significant pore pressure changes several hundreds of meters from the treatment stages (e.g., Davies *et al.*, 2012; 2013).

Despite the close lateral proximity of the CHW and CS, there is a significant depth differential between CHW stages and basement seismicity (Figs. 4b,c and 5a). Hydrologically, pressure fronts traversing vertical, impermeable and/or unfractured strata require significant time (∼decades) to diffuse; however, observed delay times on the order of hours would require a quicker route of hydraulic communication into the Archean basement, that is, along the damage zone of a mechanically active fault (e.g., Zhang *et al.*, 2013). For example, other studies have noted similar distances (∼kilometers) and delay times (∼hours) between stimulation interval and induced events (e.g., Holland, 2013; Clarke *et al.*, 2014; Friberg *et al.*, 2014; Schultz, Stern, Novakovic, *et al.*, 2015; Skoumal *et al.*, 2015).

Directly analogous to our study, microseismic monitoring at the Etsho field in the Horn River Basin observed deep-seated fault pathways from the Horn River Group HF interval to the basement (BC Oil and Gas Commission, 2012). In our study, the inference of the WSOF from formation offsets in Upper Cretaceous marine formations (Fig. 6) provides evidence of faulted bedrock structure, which is tectonically analogous to the adjacent, regional fault systems (F1–F5) (Lemieux, 1999; Zaitlin *et al.*, 2011). Local to the CHW, pre-existing

faults nearby the WSOF likely provide a candidate route of pressure migration from the Devonian–Mississippian-age Exshaw into the crystalline basement. Furthermore, lineaments inferred from gravity anomaly data are consistent with the continuation of the WSOF system into the Archean basement (Fig. 7). Thus, the CHW pressure front diffusing through stimulated fractures would likely encounter the nearby WSOF system and propagate into the basement, nucleating events at a zone of fault weakness at ~4.28 km depth. A rough computation, based on the constrained time and distance parameters (Shapiro *et al.*, 1997), would indicate an apparent, average hydraulic diffusivity ranging between 4.5 and 64 m^2/s, roughly consistent with other crustal observations (e.g., Parotidis *et al.*, 2004).

It is well understood that pore pressure has the capacity to initiate shear rupture on a fault, and the continued escalation of pressure has been modeled to understand the multiplicity of induced events (e.g., Goertz-Allmann and Wiemer, 2012) as observed in the CS. Often, models and explanations of induced seismicity assume pre-existing faults, which are both critically stressed and favorably oriented. Although a lack of data for high-resolution structural-geology interpretations limits our ability to definitively comment if any faults are in a critical state, focal mechanism and *in situ* stress considerations allow us to make some inferences on the current tectonic stress regime. Today, regions of the WCSB with seismic activity appear to be in a compressive state: a regime favoring reverse and strike-slip faulting from focal mechanism considerations (Ristau *et al.*, 2007). Regional studies of the *in situ* stress (Bell and Grasby, 2012) determined from borehole data (Schmitt *et al.*, 2012) are consistent with our moment tensor inversion, which is indicative of normal style faulting (Fig. 5).

This observation is further corroborated by our best estimates of *b*-value (1.11 ± 0.17), which has been shown as inversely proportional to differential stress on a fault with *b*-values higher than 1.0, indicating normal faulting (Schorlemmer *et al.*, 2005). Despite these consistencies, our seismically inferred *B*-axis azimuth of $12° \pm 15°$ differs from the regionally determined S_H direction of ~50° (Reiter *et al.*, 2014). However, we also note that moment tensors from reactivated faults can vary from the orientation of stress axes (McKenzie 1969), especially in a state of high pore pressure (Célérier, 1988). Second, we reconcile the relative differences in strikes between the WSOF (~155°), basement fault from potential field data (~167°), and moment tensor (12°/203°) as a result of the complexity of faulting propagation from basement into the sedimentary sequence during its extensional tectonic genesis (Lemieux, 1999). However, a thorough examination of this interpretation would require higher-resolution geophysical surveys.

Conclusions

The development of seismic monitoring capacity in the WCSB has allowed for better understanding of earthquakes, both natural and induced, in the region. In this study, we found that the events clustered at the CS are strongly correlated (> 99.7% confidence) to the treatment stages at a nearby horizontal well. Since the HF of this well, more than 60 small earthquakes have been detected near the CHW, a previously quiescent region. In terms of lateral offsets, these events are located in close proximity (~300 m) to the suspected well, although the depths of CS earthquakes are observed within the crystalline basement. We interpret the delay time (1.5–3.0 hrs) between HF stages and respondent seismicity as the propagation time of the pore-pressure front from the Exshaw Formation to the crystalline basement. Furthermore, the detection of a nearby, regional-scale fault system provides a reasonable means of hydraulic communication from the stimulated target reservoir, into the Archean basement. Moment tensor analysis suggests that the nucleated events are the reactivation of a pre-existing basement normal fault. Overall, we present a case that describes a geologically plausible scenario in which pore pressure diffuses from the HF stages of the CHW to an inferred zone of fault weakness.

Finally, we conclude that seismicity at the CS is consistent with phenomenology associated with fluid-injection-induced earthquakes, and we assert it is the most likely explanation for the origin of these events. Despite these consistencies, we do note that events detected during March 2012 (Fig. 2a) would have occurred during flowback operations at the CHW. These events provide a sobering reminder of the complexity of induced seismicity, because explaining their rupture initiation would potentially require a more complete understanding of the local stress perturbations. Also, future high-resolution studies are warranted for better understanding of the influence of HF on faulted basement near the CHW, to elucidate the geologic considerations of the CS and benefit the understanding of induced seismicity in general.

Data and Resources

Many geophysical stratigraphic tops were picked, refined, and reviewed by Shilong Mei; however, nontrivial contributions for the Milk River Formation (Glombick and Mumpy, 2014) and base of Fish Scales zone (IHS AccuMap) came from additional sources. Geostatistical elements of the bedrock offset mapping were performed using ArcGIS Geostatistical Analyst. Additionally, Jessica Dongas's work as a summer student at the Alberta Geological Survey provided the sedimentary component of our seismic velocity model. Moment tensors were computed using the mtpackagev3.0 package developed by Douglas Dreger and Sean Ford of the Berkley Seismological Laboratory, and Green's functions were computed using the FKRPROG software developed by Chandan Saikia. Background SPOT6 satellite imagery used in the figures was licensed by BlackBridge Geomatics Corp. (www.blackbridge.com, last accessed May 2015). Seismic waveform data were amalgamated from various networks, including the Canadian Rockies and Alberta Network (Gu *et al.*, 2011), the Alberta Telemetered Seismic Network (Eaton, 2014), the Montana Regional Seismic Network (D'Alessan-

dro and Stickney, 2012), and the Canadian National Seismic Network.

Acknowledgments

We would like to thank Doug Schmitt for his insights and time spent discussing geomechanical considerations of induced seismicity. In addition, we would like to thank both Art McGarr and Paul Friberg for their helpful comments in review of the manuscript.

References

Aki, K. (1965). Maximum likelihood estimate of b in the formula $\log(N) = a - bM$ and its confidence limits, *Bull. Earthq. Res. Inst. Tokyo Univ.* **43,** 237–239.

Baisch, S., L. Ceranna, and H. Harjes (2008). Earthquake cluster: What can we learn from waveform similarity? *Bull. Seismol. Soc. Am.* **98,** 2806–2814, doi: 10.1785/0120080018.

BC Oil and Gas Commission (2012). Investigation of observed seismicity in the Horn River basin, 29 pp., http://www.bcogc.ca/document.aspx?documentID=1270 (last accessed September 2014).

BC Oil and Gas Commission (2014). Investigation of observed seismicity in the Montney trend, 32 pp., http://www.bcogc.ca/sites/default/files/documentation/technical-reports/investigation-observed-seismicity-montney-trend.pdf (last accessed June 2015).

Beaumont, C., G. M. Quinlan, and G. S. Stockmal (1993). The evolution of the Western Interior basin: Causes, consequences and unsolved problems, *Spec. Pap. Geol. Assoc. Canada* **39,** 91–117.

Bell, J. S., and S. E. Grasby (2012). The stress regime of the Western Canadian sedimentary basin, *Geofluids* **12,** no. 2, 150–165, doi: 10.1111/j.1468-8123.2011.00349.x.

Célérier, B. (1988). How much does slip on a reactivated fault plane constrain the stress tensor? *Tectonics* **7,** no. 6, 1257–1278, doi: 10.1029/TC007i006p01257.

Chen, Y., Y. J. Gu, R. M. H. Dohkt, and M. D. Sacchi (2015). Crustal imprints of Precambrian orogenesis in western Laurentia, *J. Geophys. Res.* **120,** doi: 10.1002/2014JB011353.

Chen, Z., S. E. Grasby, and K. G. Osadetz (2011). Geological controls on regional transmissivity anisotropy, *Geofluids* **11,** no. 2, 228–241, doi: 10.1111/j.1468-8123.2011.00334.x.

Clarke, H., L. Eisner, P. Styles, and P. Turner (2014). Felt seismicity associated with shale gas hydraulic fracturing: The first documented example in Europe, *Geophys. Res. Lett.* **41,** 8308–8314, doi: 10.1002/2014GL062047.

D'Alessandro, A., and M. Stickney (2012). Montana seismic network performance: An evaluation through the SNES method, *Bull. Seismol. Soc. Am.* **102,** no. 1, 73–87, doi: 10.1785/0120100234.

Davies, R., G. Foulger, A. Bindley, and P. Styles (2013). Induced seismicity and hydraulic fracturing for the recovery of hydrocarbons, *Mar. Petrol. Geol.* **45,** 171–185, doi: 10.1016/j.marpetgeo.2013.03.016.

Davies, R. J., S. A. Mathias, J. Moss, S. Hustoft, and L. Newport (2012). Hydraulic fractures: How far can they go? *Mar. Petrol. Geol.* **37,** no. 1, 1–6, doi: 10.1016/j.marpetgeo.2012.04.001.

Davis, S. D., and C. Frohlich (1993). Did (or will) fluid injection cause earthquakes? Criteria for a rational assessment, *Seismol. Res. Lett.* **64,** 207–224.

Downie, R., E. Kronenberger, and S. C. Maxwell (2010). Using microseismic source parameters to evaluate the influence of faults on fracture treatments: A geophysical approach to interpretation, *SPE Annual Technical Conference and Exhibition*, Florence, Italy, 19–22 September, Society of Petroleum Engineers, doi: 10.2118/134772-MS.

Dreger, D. S. (2003). TDMT_INV: Time Domain seismic Moment Tensor INVersion, in *International Handbook of Earthquake Engineering Seismology*, Vol. 81B, Academic Press, London, United Kingdom, 1627 pp.

Earthquakes Canada (2014). GSC, earthquake search (online bulletin), *Nat. Res. Can.*, available at http://earthquakescanada.nrcan.gc.ca/stndon/NEDB-BNDS/bull-eng.php (last accessed December 2014).

Eaton, D. (2014). Alberta Telemetered Seismograph Network (ATSN): Real-time monitoring of seismicity in northern Alberta, *CSEG Recorder* **39,** no. 3, 30–33.

Eaton, D., and A. Babaie Mahani (2015). Focal mechanisms of some inferred induced earthquakes in Alberta, Canada, *Seismol. Res. Lett.* **86,** 1078–1085, doi: 10.1785/0220150066.

Efron, B., and R. Tibshirani (1986). Bootstrap methods for standard errors, confidence intervals, and other measures of statistical accuracy, *Stat. Sci.* 54–75, doi: 10.1214/ss/1177013815.

Ellsworth, W. L. (2013). Injection-induced earthquakes, *Science* **341,** 6142, doi: 10.1126/science.1225942.

Fischer, T., and A. Guest (2011). Shear and tensile earthquakes caused by fluid injection, *Geophys. Res. Lett.* **38,** no. 5, doi: 10.1029/2010GL045447.

Friberg, P. A., G. M. Besana-Ostman, and I. Dricker (2014). Characterization of an earthquake sequence triggered by hydraulic fracturing in Harrison County, Ohio, *Seismol. Res. Lett.* **85,** no. 2, 462, doi: 10.1785/0220140127.

Frohlich, C. (2001). Display and quantitative assessment of distributions of earthquake focal mechanisms, *Geophys. J. Int.* **144,** no. 2, 300–308, doi: 10.1046/j.1365-246x.2001.00341.x.

Glombick, P, and A. J. Mumpy (2014). Subsurface stratigraphic picks for the Milk River "shoulder," Alberta Plains: Including tops for the Milk River Formation and Alderson member of the Lea Park Formation; Alberta Energy Regulator, *AER/AGS Open-File Rept. 2013-17*, 23 pp.

Goertz-Allmann, B. P., and S. Wiemer (2012). Geomechanical modeling of induced seismicity source parameters and implications for seismic hazard assessment, *Geophysics* **78,** no. 1, KS25–KS39, doi: 10.1190/geo2012-0102.1.

Gregory, K. B., R. D. Vidic, and D. A. Dzombak (2011). Water management challenges associated with the production of shale gas by hydraulic fracturing, *Elements* **7,** no. 3, 181–186, doi: 10.2113/gselements.7.3.181.

Gu, Y. J., A. Okeler, L. Shen, and S. Contenti (2011). The Canadian Rockies and Alberta Network (CRANE): New constraints on the Rockies and western Canada sedimentary basin, *Seismol. Res. Lett.* **82,** 575–588, doi: 10.1785/gssrl.82.4.575.

Hamilton, W. N., C. W. Langenberg, M. Price, and D. K. Chao (2012). Major bedrock faults of Alberta, GIS data (line features) shown on AGS Map 236, Energy Resources Conservation Board, ERCB/AGS Digital Data 2012-0016, http://www.ags.gov.ab.ca/publications/abstracts/DIG_2012_0016.html (last accessed January 2015).

Healy, J. T., W. W. Rubey, D. T. Griggs, and C. B. Raleigh (1968). The Denver earthquakes, *Science* **161,** 1301–1310, doi: 10.1126/science.161.3848.1301.

Hiebert, S. N., and D. A. Spratt (1996). Geometry of the thrust front near Pincher Creek, Alberta, *Bull. Can. Petrol. Geol.* **44,** no. 2, 195–201.

Hildebrand, R. S. (2013). Mesozoic assembly of the North American cordillera, *Geol. Soc. Am. Spec. Pap.* **495,** 169 pp.

Holland, A. A. (2013). Earthquakes triggered by hydraulic fracturing in south-central Oklahoma, *Bull. Seismol. Soc. Am.* **103,** 1784–1792, doi: 10.1785/0120120109.

Horner, R. B., J. E. Barclay, and J. M. MacRae (1994). Earthquakes and hydrocarbon production in the Fort St. John area of northeastern British Columbia, *Can. J. Explor. Geophys.* **30,** no. 1, 39–50.

Hsieh, P. A., and J. D. Bredehoeft (1981). A reservoir analysis of the Denver earthquakes: A case of induced seismicity, *J. Geophys. Res.* **86,** no. B2, 903–920, doi: 10.1029/JB086iB02p00903.

Hubbert, M. K., and W. W. Rubey (1959). Role of fluid pressure in mechanics of overthrust faulting I. Mechanics of fluid-filled porous solids and its application to overthrust faulting, *Bull. Geol. Soc. Am.* **70,** no. 2, 115–166, doi: 10.1130/0016-7606(1959)70[115:ROFPIM]2.0.CO;2.

Irish, E. J. W. (1968). Lethbridge, Alberta, *Geological Survey of Canada, Map 20-1967*, 1:253,440 scale.

Kim, W. Y. (2013). Induced seismicity associated with fluid injection into a deep well in Youngstown, Ohio, *J. Geophys. Res.* **118,** no. 7, 3506–3518, doi: 10.1002/jgrb.50247.

King, G. E. (2010). Thirty years of gas shale fracturing: What have we learned? *SPE Annual Technical Conference and Exhibition*, Florence, Italy, 19–22 September, Society of Petroleum Engineers, doi: 10.2118/133456-MS.

Laske, G., G. Masters, Z. Ma, and M. Pasyanos (2013). Update on CRUST1.0: A 1-degree global model of Earth's crust, *EGU General Assembly Conference Abstracts*, Vienna, Austria, 7–12 April 2013, Vol. 15**,** 2658 pp.

Lemieux, S. (1999). Seismic reflection expression and tectonic significance of Late Cretaceous extensional faulting of the Western Canada sedimentary basin in southern Alberta, *Bull. Can. Petrol. Geol.* **47,** no. 4, 375–390.

Lemieux, S., G. M. Ross, and F. A. Cook (2000). Crustal geometry and tectonic evolution of the Archean crystalline basement beneath the southern Alberta Plains, from new seismic reflection and potential-field studies, *Can. J. Earth Sci.* **37,** no. 11, 1473–1491, doi: 10.1139/e00-065.

Lyatsky, H., D. Pană, R. Olson, and L. Godwin (2004). Detection of subtle basement faults with gravity and magnetic data in the Alberta basin, Canada: A data-use tutorial, *TLE* **23,** no. 12, 1282–1288, doi: 10.1190/leedff.23.1282_1.

Lyatsky, H. V., and D. I. Pană (2003). Catalogue of selected regional gravity and magnetic maps of northern Alberta, *Alberta Geol. Surv.*, Alberta Energy and Utilities Board.

Lyatsky, H. V., D. I. Pană, and M. Grobe (2005). Basement structure in central and southern Alberta, insights from gravity and magnetic maps, *Energy and Utilities Board (EUB)/Alberta Geol. Surv. Spec. Rept. 72*, 76 pp.

Macqueen, R. W., and C. A. Sandberg (1970). Stratigraphy, age, and interregional correlation of the Exshaw Formation, Alberta Rocky Mountains, *Bull. Can. Petrol. Geol.* **18,** no. 1, 32–66.

Majer, E. L., R. Baria, M. Stark, S. Oates, J. Bommer, B. Smith, and H. Asanuma (2007). Induced seismicity associated with enhanced geothermal systems, *Geothermics* **36,** no. 3, 185–222, doi: 10.1016/j.geothermics.2007.03.003.

Maxwell, S. C., and C. L. Cipolla (2011). What does microseismicity tell us about hydraulic fracturing? *SPE Annual Technical Conference and Exhibition*, Denver, Colorado, 30 October–2 November, Society of Petroleum Engineers, doi: 10.2118/146932-MS.

Maxwell, S. C., M. Jones, R. Parker, S. Leaney, M. Mack, D. Dorvall, D. D'Amico, J. Logel, E. Anderson, and K. Hammermaster (2010). Fault activation during hydraulic fracturing, *72nd EAGE Conference and Exhibition*, Barcelona, Spain, 14 June.

McGarr, A. (2014). Maximum magnitude earthquakes induced by fluid injection, *J. Geophys. Res.* **119,** no. 2, 1008–1019, doi: 10.1002/2013JB010597.

McKenzie, D. P. (1969). The relation between fault plane solutions for earthquakes and the directions of the principal stresses, *Bull. Seismol. Soc. Am.* **59,** no. 2, 591–601.

Mei, S. (2009a). Geologist-controlled trends versus computer-controlled trends: Introducing a high-resolution approach to subsurface structural mapping using well-log data, trend surface analysis, and geospatial analysis, *Can. J. Earth Sci.* **46,** no. 5, 309–329, doi: 10.1139/E09-024.

Mei, S. (2009b). New insights on faults in the Peace River arch region, northwest Alberta, based on existing well-log data and refined trend surface analysis, *Can. J. Earth Sci.* **46,** no. 1, 41–65, doi: 10.1139/E09-006.

Monger, J. W. H., and R. Price (2002). The Canadian Cordillera: Geology and tectonic evolution, *CSEG Recorder* **27,** no. 2, 17–36.

Pană, D. I., and B. A. van der Pluijm (2014). Orogenic pulses in the Alberta Rocky Mountains: Radiometric dating of major faults and comparison with the regional tectono-stratigraphic record, *Bull. Geol. Soc. Am.* no. B31069-1, doi: 10.1130/B31069.1.

Parotidis, M., S. A. Shapiro, and E. Rothert (2004). Back front of seismicity induced after termination of borehole fluid injection, *Geophys. Res. Lett.* **31,** no. 2, doi: 10.1029/2003GL018987.

Price, R. A. (1994). Cordilleran tectonics and the evolution of the Western Canada sedimentary basin, in *Geological Atlas of the Western Canada Sedimentary Basin*, G. Mossop and I. Shetsen (Editors), Canadian Society of Petroleum Geologists and Alberta Research Council, Calgary, Canada, 13–24.

Reiter, K., O. Heidbach, D. Schmitt, K. Haug, M. Ziegler, and I. Moeck (2014). A revised crustal stress orientation database for Canada, *Tectonophysics* **636,** 111–124, doi: 10.1016/j.tecto.2014.08.006.

Reyes, C. G., and M. E. West (2011). The waveform suite: A robust platform for manipulating waveforms in MATLAB, *Seismol. Res. Lett.* **82,** 104–110, doi: 10.1785/gssrl.82.1.104.

Ristau, J., G. C. Rogers, and J. F. Cassidy (2007). Stress in western Canada from regional moment tensor analysis, *Can. J. Earth Sci.* **44,** no. 2, 127–148, doi: 10.1139/e06-057.

Rokosh, C. D., S. Lyster, S. D. A. Anderson, A. P. Beaton, H. Berhane, T. Brazzoni, D. Chen, Y. Cheng, T. Mack, C. Pană, and J. G. Pawlowicz (2012). Summary of Alberta's shale- and siltstone-hosted hydrocarbon resource potential, Energy Resources Conservation Board, *Energy Resources Conservation Board (ERCB)/Alberta Geological Survey (AGS) Open-File Rept. 2012-06*, 327 pp.

Ross, G. M., and D. W. Eaton (1999). Basement reactivation in the Alberta basin: Observational constraints and mechanical rationale, *Bull. Can. Petrol. Geol.* **47,** no. 4, 391–411.

Russel, L. S., and R. W. Landes (1940). Geology of the southern Alberta Plains, *Geological Survey of Canada Memoir 221*, Department of Mines and Resources, Mines and Geology Branch, Bureau of Geology and Topography, 1–128.

Rutledge, J., R. Downie, S. Maxwell, J. Drew, and T. Fischer (2013). Extension-shear microseismic mechanisms during hydraulic fracturing, *2013 SEG Annual Meeting*, Houston, Texas, 22–27 September, Society of Exploration Geophysicists.

Saikia, C. K. (1994). Modified frequency–wavenumber algorithm for regional seismograms using Filon's quadrature: Modelling of Lg waves in eastern North America, *Geophys. J. Int.* **118,** no. 1, 142–158, doi: 10.1111/j.1365-246X.1994.tb04680.x.

Schaff, D. P (2008). Semiempirical statistics of correlation-detector performance, *Bull. Seismol. Soc. Am.* **98,** 1495–1507, doi: 10.1785/0120060263.

Schmitt, D. R., C. A. Currie, and L. Zhang (2012). Crustal stress determination from boreholes and rock cores: Fundamental principles, *Tectonophysics* **580,** 1–26, doi: 10.1016/j.tecto.2012.08.029.

Schorlemmer, D., S. Wiemer, and M. Wyss (2005). Variations in earthquake-size distribution across different stress regimes, *Nature* **437,** no. 7058, 539–542, doi: 10.1038/nature04094.

Schultz, R., V. Stern, and Y. J. Gu (2014). An investigation of seismicity clustered near the Cordel Field, west central Alberta, and its relation to a nearby disposal well, *J. Geophys. Res.* **119,** no. 4, 3410–3423, doi: 10.1002/2013JB010836.

Schultz, R., V. Stern, Y. J. Gu, and D. Eaton (2015). Detection threshold and location resolution of the Alberta Geological Survey earthquake catalog, *Seismol. Res. Lett.* **86,** no. 2A, 385–397, doi: 10.1785/0220140203.

Schultz, R., V. Stern, M. Novakovic, G. Atkinson, and Y. J. Gu (2015). Hydraulic fracturing and the Crooked Lake sequences: Insights gleaned from regional seismic networks, *Geophys. Res. Lett.* **42,** no. 8, 2750–2758, doi: 10.1002/2015GL063455.

Shapiro, S. A., E. Huenges, and G. Borm (1997). Estimating the crust permeability from fluid-injection-induced seismic emission at the KTB site, *Geophys. J. Int.* **131,** no. 2, F15–F18, doi: 10.1111/j.1365-246X.1997.tb01215.x.

Shi, Y., and B.A. Bolt (1982). The standard error of the magnitude–frequency *b* value, *Bull. Seismol. Soc. Am.* **72,** 1677–1687.

Skoumal, R. J., M. R. Brudzinski, and B. S. Currie (2015). Earthquakes induced by hydraulic fracturing in Poland Township, Ohio, *Bull. Seismol. Soc. Am.* **105,** 189–197, doi: 10.1785/0120140168.

Stern, V. H., R. J. Schultz, L. Shen, Y. J. Gu, and D. W. Eaton (2013). Alberta earthquake catalogue, version 1.0, September 2006 through December 2010, *Alberta Geol. Surv. Open-File Rept. 2013-15*, 36 pp.

Stockmal, G. S., D. Lebel, M. E. Mcmechan, and P. A. Mackay (2001). Structural style and evolution of the triangle zone and external Foothills, southwestern Alberta: Implications for thin-skinned thrust-and-fold belt mechanics, *Bull. Can. Petrol. Geol.* **49,** no. 4, 472–496.

Struik, L. C. (1988). Crustal evolution of the eastern Canadian Cordillera, *Tectonics* **7,** no. 4, 727–747, doi: 10.1029/TC007i004p00727.

Telesca, L. (2010). Analysis of the cross-correlation between seismicity and water level in the Koyna area of India, *Bull. Seismol. Soc. Am.* **100,** 2317–2321, doi: 10.1785/0120090392.

Ugalde, H. A., S. L. Underhay, W. A. Morris, and K. Markham (2008). Evidence for basement fault reactivation in southern Alberta: An integrated topography and airborne magnetics approach, *CSEG Recorder* **33,** no. 1, 1–16.

U.S. Energy Information Administration (2013). Technically recoverable shale oil and shale gas resources: An assessment of 137 shale formations in 41 countries outside the United States, U.S. Department of Energy/Energy Information Administration (EIA), Washington, D.C., 730 pp., http://www.eia.gov/analysis/studies/worldshalegas (last accessed February 2015).

Vavryčuk, V. (2015). Moment tensor decompositions revisited, *J. Seismol.* **19,** no. 1, 231–252, doi: 10.1007/s10950-014-9463-y.

Waldhauser, F., and W. L. Ellsworth (2000). A double-difference earthquakes location algorithm: Method and application to the northern Hayward fault, California, *Bull. Seismol. Soc. Am.* **90,** 1353–1368, doi: 10.1785/0120000006.

Warpinski, N. R., J. Du, and U. Zimmer (2012). Measurements of hydraulic-fracture-induced seismicity in gas shales, *SPE Prod. Operations* **27,** no. 3, 240–252, doi: 10.2118/151597-PA.

Waters, G., H. Ramakrishnan, J. Daniels, D. Bentley, J. Belhadi, and M. Ammerman (2009). Utilization of real time microseismic monitoring and hydraulic fracture diversion technology in the completion of Barnett shale horizontal wells, presented at *The Offshore Technology Conference*, Houston, Texas, paper OTC 20268, 4–7.

Wessel, P., and W. H. Smith (1998). New, improved version of Generic Mapping Tools released, *Eos Trans. AGU* **79,** no. 47, 579–579, doi: 10.1029/98EO00426.

Wessels, S. A., A. De La Pena, M. Kratz, S. Williams-Stroud, and T. Jbeili (2011). Identifying faults and fractures in unconventional reservoirs through microseismic monitoring, *First Break* **29,** no. 7, 99–104.

Wright, G. N., M. E. McMechan, and D. E. G. Potter (1994). Structure and architecture of the Western Canada sedimentary basin, in *Geological Atlas of the Western Canada Sedimentary Basin*, G. D. Mossop and I. Shetsen (Editors), Alberta Research Council, Edmonton, Alberta, 25–40.

Yang, Y., M. Zoback, M. Simon, and T. Dohmen (2013). An integrated geomechanical and microseismic study of multi-well hydraulic fracture stimulation in the Bakken Formation, *Unconventional Resources Technology Conference*, Denver, Colorado, 12–14 August, Society of Petroleum Engineers, doi: 10.1190/URTEC2013-056.

Zaitlin, B., J. Kennedy, and S. Kehoe (2010). The Alberta Bakken: A new, unconventional tight oil resource play, *BMO Capital Markets Oil and Gas Report*, 21 pp.

Zaitlin, B., W. S. Low, J. Kennedy, and S. Kehoe (2011). BMO technical update: The Alberta Bakken petroleum system (ABPS) is "steady as she goes" an emerging unconventional tight oil resource play, *BMO Capital Markets Oil and Gas Report*, 34 pp.

Zhang, Y., M. Person, J. Rupp, K. Ellett, M. A. Celia, C. W. Gable, B. Bowen, J. Evans, K. Bandilla, P. Mozley, *et al.* (2013). Hydrogeologic controls on induced seismicity in crystalline basement rocks due to fluid injection into basal reservoirs, *Groundwater* **51,** no. 4, 525–538, doi: 10.1111/gwat.12071.

Alberta Geological Survey
402 Twin Atria Building
4999 98 Avenue
Edmonton, Alberta
Canada T6B 2X3
ryan.schultz@aer.ca
rjs10@ualberta.ca
(R.S., S.M., D.P., V.S.)

University of Alberta
116 Street 85 Avenue
Edmonton, Alberta
Canada T6G 253
(Y.J.G.)

Yokohoma City University
22-2 Seto
Kanazawa Ward, Yokohoma
Kanagawa Prefecture 236-0027
Japan
(A.K.)

University of Calgary
2500 University Drive NW
Calgary, Alberta
Canada T2N 1N4
(D.E.)

Manuscript received 29 May 2015;
Published Online 10 November 2015